Unstructured grid based 2D inversion of plane wave EM data for models including topography

Baranwal, V.C.[1,2], Franke, A.[1], Börner, R.-U.[1], Spitzer, K.[1]

[1] Institute of Geophysics, Technische Universität Bergakademie Freiberg, Freiberg, Germany

[2] now at University of Southampton, UK

SUMMARY

We present a 2D damped least-squares inversion code for plane wave electromagnetic (EM) methods using an adaptive unstructured grid finite element forward operator. Unstructured triangular grids permit efficient discretization of arbitrary 2D model geometries and, hence, allow for modeling arbitrary topography. The inversion model is parameterized on a coarse parameter grid which constitutes a subset of the forward modeling grid. We investigate two types of parameter grids: a regular type, however, containing trapezoidal cells and hanging nodes, and an unstructured triangular type. The transformation from parameter to forward modeling grid is obtained by adaptive mesh refinement. Sensitivities are determined by solving a modified sensitivity equation system obtained from the derivative of the finite element equations with respect to the model parameters.

Firstly, the inversion of a COPROD2 data set in E-polarization is presented as an example to show that our inversion code produces reasonable results for real data and flat earth models. Secondly, we demonstrate that surface topography may induce significant effects on the EM response and the inversion result, and that it cannot be ignored when the scale length of topographic variations is in the order of magnitude of the skin depth. Finally, we demonstrate the inversion of a synthetic data set from a model with topography.

Keywords: Unstructured grids, finite elements, topography, VLF, MT, inversion

---

FORWARD MODELING

The forward computations are carried out using an adaptive unstructured triangular grid finite element algorithm (Franke, Börner and Spitzer, 2004). In the case of plane, diffusive, time-harmonic electromagnetic fields in 2D conductivity structures Maxwell's equations can be combined to yield two decoupled equations of induction reading

$$\frac{\partial^2 E_y}{\partial^2 x^2} + \frac{\partial^2 E_y}{\partial^2 z^2} = i\omega\mu\sigma E_y, \tag{1}$$

$$\frac{\partial}{\partial x}\left(\frac{1}{\sigma}\frac{\partial H_y}{\partial x}\right) + \frac{\partial}{\partial z}\left(\frac{1}{\sigma}\frac{\partial H_y}{\partial z}\right) = i\omega\mu H_y \tag{2}$$

for E- and H-polarizations, respectively, in a right-handed Cartesian coordinate system with the positive z-axis pointing upwards. E_y is the y-component of the electric field and H_y is the y-component of the magnetic field. y denotes the strike direction. ω, μ, i, and σ are angular frequency, magnetic permeability, imaginary unit, and electrical conductivity, respectively. To solve for the unknown fields, inhomogeneous Dirichlet boundary conditions are applied that assign the field values of a horizontally layered half-space to the boundaries.

The finite element discretization leads to a system of equations that can be expressed in matrix-vector form as

$$(\mathbf{K} + \mathbf{M})\,\vec{u} = f, \tag{3}$$

where $\vec{u}$ is either a column vector of the electric field E_y or the magnetic field H_y at each node in E- and H-polarization, respectively, and f is the right-hand side. $\mathbf{K}$ and $\mathbf{M}$ are referred to as stiffness and mass matrices.

The remaining field components H_x, H_z for E-polarization and E_x, E_z for H-polarization can be determined at each grid node by

$$H_x = \frac{1}{i\omega\mu}\frac{\partial E_y}{\partial z}, \quad \text{and} \quad H_z = -\frac{1}{i\omega\mu}\frac{\partial E_y}{\partial x},$$

$$E_x = -\frac{1}{\sigma}\frac{\partial H_y}{\partial z}, \quad \text{and} \quad E_z = \frac{1}{\sigma}\frac{\partial H_y}{\partial x}. \tag{4}$$

The apparent resistivity ρ_a and the phase ϕ for E- and H-polarizations (in the case of VLF-R and MT methods) can be computed as

$$\rho_a = \frac{1}{\omega\mu}\left|\frac{E_y}{H_x}\right|^2, \phi = \tan^{-1}\left(\frac{\text{imag}\,(E_y/H_x)}{\text{real}\,(E_y/H_x)}\right), \tag{5}$$
$$\text{for E-polarization,}$$

$$\rho_a = \frac{1}{\omega\mu}\left|\frac{E_x}{H_y}\right|^2, \phi = \tan^{-1}\left(\frac{\text{imag}\,(E_x/H_y)}{\text{real}\,(E_x/H_y)}\right), \tag{6}$$
$$\text{for H-polarization.}$$

The real part Re and the imaginary part Im of the magnetic transfer function in the case of VLF can be computed as

$$Re = \text{real}\left(\frac{H_z}{H_x}\right)\cdot 100\%,$$
$$Im = \text{imag}\left(\frac{H_z}{H_x}\right)\cdot 100\% \tag{7}$$

INVERSION PROCEDURE

We apply a damped least-squares method for the minimization of the objective function ψ given by

$$\psi = \left(\Delta\vec{d} - \mathbf{S}\Delta\vec{p}\right)^T\left(\Delta\vec{d} - \mathbf{S}\Delta\vec{p}\right)$$
$$+ \lambda\left(\Delta\vec{p}^T\Delta\vec{p} - p_0^2\right), \tag{8}$$

where $\Delta\vec{d} = \vec{d}^{obs} - \vec{d}^{comp}$ describes the discrepancy between the observed data $\vec{d}^{obs}$ and the computed data $\vec{d}^{comp}$. $\mathbf{S}$ and $\Delta\vec{p}$ denote the sensitivity matrix and the model parameter update, respectively. The logarithm of the conductivities are considered as model parameters. The Lagrange parameter λ is introduced to constrain the energy of the model parameter update to a finite quantity p_0^2. To get the minimum of the objective function ψ, its partial derivatives $\partial\psi/\partial\Delta p_j$ are required to be zero for all model cells j. The resulting normal equation reads

$$\left(\mathbf{S}^T\mathbf{S} + \lambda\mathbf{I}\right)\Delta\vec{p} = \mathbf{S}^T\Delta\vec{d}, \tag{9}$$

where $\mathbf{I}$ is the identity matrix. Equation (9) is solved applying a direct solver at each stage of the iterative inversion process. Model parameters are updated in each iteration. In the first step of our approach, we find that the maximum singular value of $\mathbf{S}^T\mathbf{S}$ proves to be a good guess as the starting value for the Lagrange parameter λ. To get fast convergence, λ is decreased by a factor of less than one (e.g. 0.6) in each iteration.
The root mean square (RMS) error and χ^2-value can be calculated by

$$RMS = \sqrt{\frac{1}{n}\sum_{i=1}^{n}\Delta d_i{}^2},$$
$$\chi^2 = \frac{1}{n}\sum_{i=1}^{n}\frac{\Delta d_i{}^2}{\epsilon_i^2}, \tag{10}$$

where ϵ_i and n denote the standard deviation of the data and number of the data, respectively. We stop the iteration if one of the following criteria is met: (1) the maximum number of iterations is reached, (2) the convergence of RMS error stagnates, (3) $\chi^2 \approx 1$.

SENSITIVITY CALCULATION

The element S_{ij} of the sensitivity matrix $\mathbf{S}$ for the ith observation site and j^{th} model parameter is calculated using the modified sensitivity equation method presented by Rodi (1976) which requires $(n + 1)$ forward computations for each

frequency

$$S_{ij} = \left(\frac{\vec{a_i}}{\vec{a_i}^T \vec{u}} - \frac{\vec{b_i}}{\vec{b_i}^T \vec{u}} \right) (\mathbf{K} + \mathbf{M})^{-1}$$
$$\left(-\frac{\partial(\mathbf{K} + \mathbf{M})}{\partial(\ln \sigma_j)} \right) \vec{u},$$

(11)

where $\vec{a_i}$ and $\vec{b_i}$ are column vectors to calculate the electric and the magnetic fields in the case of E-polarization and vice-versa in the case of H-polarization for the ith datum from $\vec{u}$. $\vec{a_i}$ is formed by simply keeping 1 at the position of the ith datum and zeros at the other nodes. If the observation site is not located exactly at grid node then field values are interpolated by two nearby grid nodes. $\vec{b_i}$ is designed in such a way that it performs a numerical differentiation over $\vec{u}$ according to eq. (4).

The sensitivities for the logarithm of the apparent resistivity $S_{ij}^{\ln \rho_a}$ and for the phase S_{ij}^{ϕ} can be computed as follows:

$$S_{ij}^{\ln \rho_a} = 2 \operatorname{real}(S_{ij}) \quad , \quad S_{ij}^{\phi} = \operatorname{imag}(S_{ij}).$$

(12)

An analogous strategy is used to calculate sensitivities for the real and imaginary parts of the magnetic transfer function in the case of VLF that corresponds to the E-polarization case. The only difference is that $\vec{a_i}$ and $\vec{b_i}$ both are now designed to perform numerical differentiation over $\vec{u}$ to get H_z and H_x according to eq. (4).

For details of these derivations, the reader is referred to Rodi (1976) and Farquharson and Oldenburg (1996).

### INVERSION OF A FLAT EARTH COPROD2 DATA SET

In this section, we show that our code is basically working for real field data, however, for reasons of comparability and due to the lack of available examples we restrict ourselves to a flat target area. We therefore invert, as an example, a COPROD2 data set (Jones, 1993) consisting of 20 sites and 4 periods in E-polarization to show that our code produces results comparable to other flat earth inversion codes. Here we have chosen the Occam inversion code by deGroot-Hedlin and Constable (1993). Fig. 1a shows our inverted model obtained in 15 iterations starting from a $100\,\Omega{\cdot}\mathrm{m}$ half-space. The χ^2-value is 1.1 when the error floor is set to 10% in ρ_a and $2.9°$ in ϕ. The presence of a conductive overburden down to $5\,\mathrm{km}$ depth and three distinct anomalous regions below 10 to $50\,\mathrm{km}$ depth are clearly visible. Fig. 1b shows the inverted model using the Occam code starting from the same half-space model and assuming the same error floor, however, considering the data from both E- and H- polarizations. Both results agree well.

### PARAMETERIZATION OF A MODEL INCLUDING SURFACE TOPOGRAPHY

In the following, we discuss two possibilities of parameterizing a model whose surface is associated with a varying topography. We perform the parameterization by segmentation either in rectangles and trapezoids (Fig. 2) that form a rather regular type of grid or in unstructured triangular cells (Fig. 3) that closely correspond to the forward modeling grid. The rectangular/trapezoidal grid comprises hanging nodes which enhance the flexibility with respect to resolution. Both types are adaptively refined into unstructured triangular grids for forward modeling. In Figs 2 and 3, the parameter grid is indicated in red and the first refinement stage of the unstructured triangular forward modeling grid in blue. Note that the latter is further refined using an adaptive refinement strategy to actually perform the simulation.

THE TOPOGRAPHY EFFECT

We now investigate the influence of the topography on the VLF-R and VLF response and the inverse process. For this purpose, we disassemble a model in a first step to separately examine its response originating from the subsurface and from topographic undulations. Since these features are inductively coupled, both superposed responses are certainly not giving the total response. However, it instructively displays the order of magnitude of the associated effects. In a second
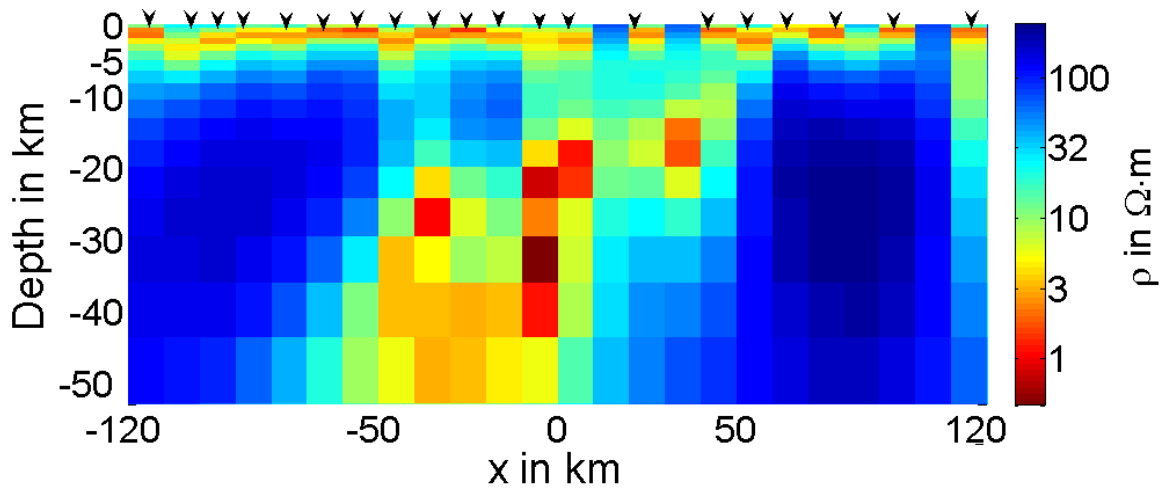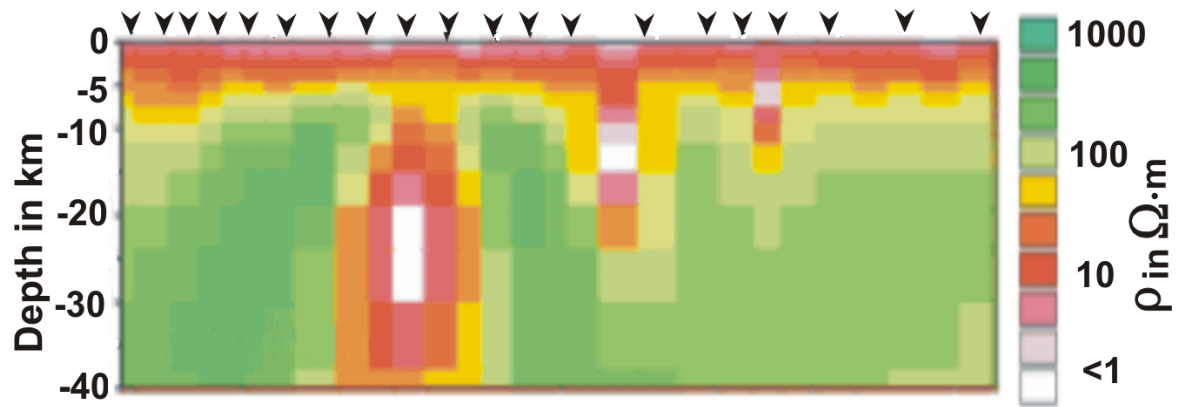
Figure 1: (a) Model obtained from the inversion of the COPROD2 data in E-polarization using the inversion code presented here. (b) Model obtained from a smoothness-constrained joint inversion of the COPROD2 data in E- and H-polarizations according to deGroot-Hedlin and Constable (1993) (modified after Jones, 1993).

step, we take data of a homogeneous earth model with surface topography and perform a flat earth inversion to point out topography induced artifacts.

DECOMPOSING THE RESPONSE FROM SURFACE TOPOGRAPHY AND SUBSURFACE CONDUCTIVITY STRUCTURES

The synthetic model displayed in Fig. 4 consists of two anomalous regions having resistivities of $100\,\Omega\cdot$m and $20\,\Omega\cdot$m, respectively, within a $1000\,\Omega\cdot$m half-space with a smooth, but pronounced topography. The observation sites are located at $50\,$m intervals from $-575\,$m to $575\,$m and marked by arrows. Synthetic data are generated for three frequencies in the VLF range: 5, 16 and $25\,$kHz. In Fig. 4a, the total synthetic response of the complete model is displayed in terms of apparent resistivity and phase according to eq. 6 and real and imaginary part of the magnetic transfer function according to eq. 7. In Fig. 4b, the perturbing bodies are removed so that a homogeneous model remains. The response clearly shows the influence of the topography. In Fig. 4c, the topography undulations are replaced by an average flat earth level so that the remaining lateral variation in the response is only due to the perturbing bodies. Note that the order of magnitude of both effects is comparable.
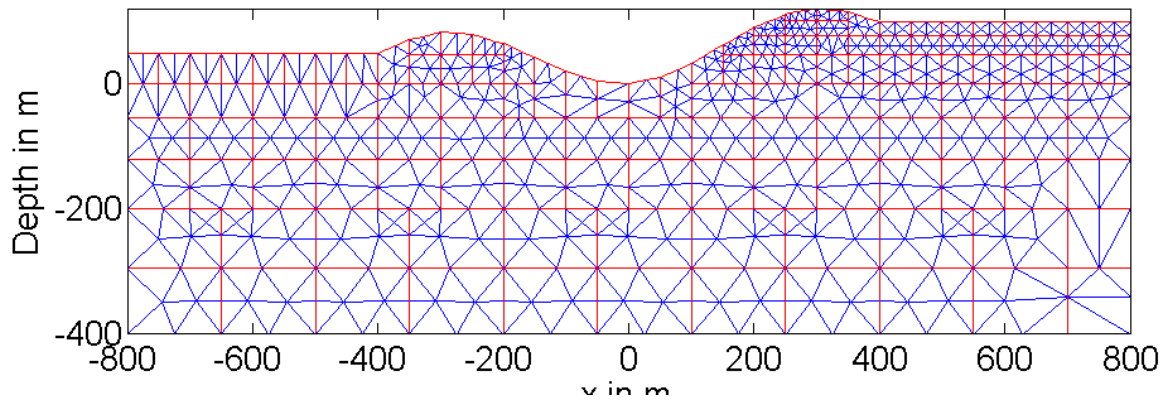
Figure 2: Parameterizing the model in rectangles and trapezoids (red lines). The unstructured forward modeling grid is indicated in blue.
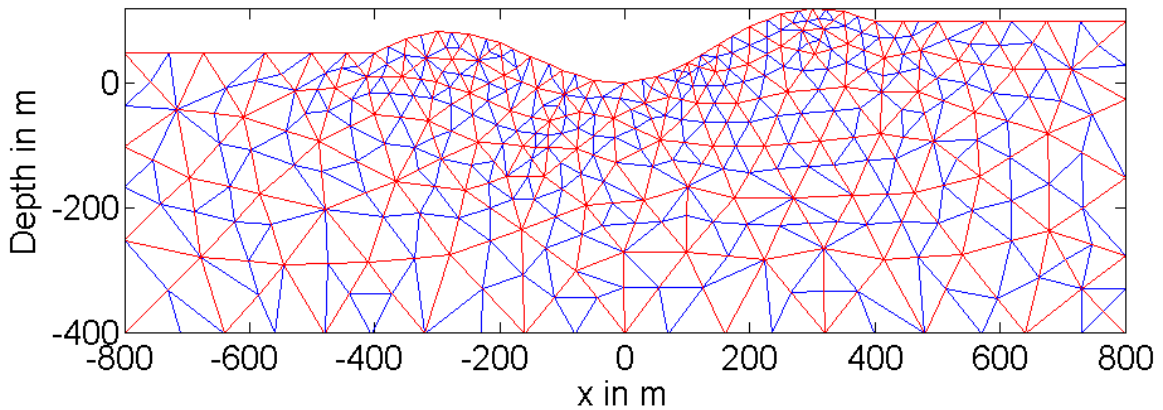

Figure 3: Parameterizing the model in unstructured triangular grids (red lines). The forward modeling grid is again outlined in blue.

FLAT EARTH INVERSION OF DATA FROM MODELS WITH TOPOGRAPHY

In this section we investigate how data from a model with topography influence the results of our inversion algorithm if the topography is not taken into account. For this purpose, we consider the synthetic VLF-R data set shown in Fig. 4b which is generated for a homogeneous $1000\,\Omega{\cdot}m$ model with topography and without anomalous regions. We invert this data set using a flat earth assumption. The starting model is a $2000\,\Omega{\cdot}m$ half-space. The inversion result obtained in 11 iterations is shown in Fig. 5. There are clear artifacts associated with the topography undulations. Conductive structures having resistivities of $\approx 500\,\Omega{\cdot}m$ appear below the central valley and the transitions from the hills to the planes on the left- and right-hand side whereas resistive anomalies around $2500\,\Omega{\cdot}m$ show up beneath the hills. Knowing the true resistivity, the maximum deviation of the inverted resistivities is more than a factor of 2 in both directions of the resistivity scale.

This example demonstrates that the topography effect may become significant. It is therefore necessary to take into account any arbitrary topography for simulation and inversion. Approximate data correction schemes then become needless.
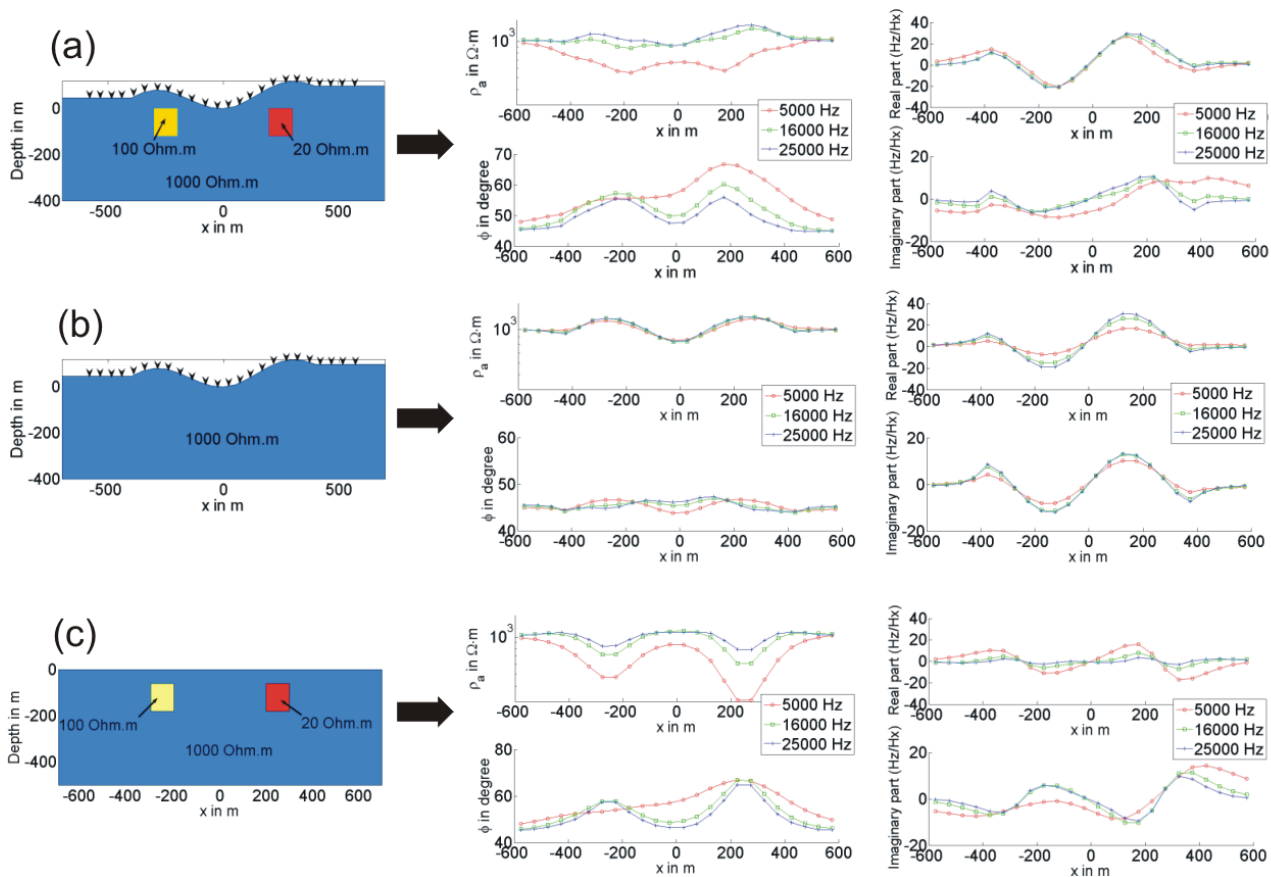
Figure 4: Synthetic responses for different models: (a) with topography and conductive regions (b) only with topography and (c) only with conductive regions within a flat earth.

INVERSION OF SYNTHETIC DATA FROM MODELS INCLUDING TOPOGRAPHY

To show that our code is able to cope with the problem of topography induced artifacts we take the synthetic data set from Fig. 4a for both the VLF-R and VLF case and add 5% random noise for each frequency. We invert these data using both parameterization schemes presented in Figs 2 and 3. Starting model is always a homogeneous $2000\,\Omega\cdot$m model.

For brevity, we are only going to show here the resulting models obtained by inversion of VLF-R data (Figs 6 and 7). The original rectangular anomalous regions are indicated by dashed lines. Both parameterization schemes recover the synthetic models satisfactorily after reaching the χ^2-criterion (in 8 to 9 iteration steps).

At first glance, the parameterization using rectangles and trapezoids seems to give better results in comparison with the parameterization using unstructured grids. This, however, is due to the perfect match of structure and grid. The future strategy is to adapt unstructured grids in each iteration step to some arbitrary structure obtained during the inversion process.

CONCLUSIONS

We have developed a 2D inversion code for inverting plane wave EM data from models including topography. At first, we have shown that our inversion code is able to cope with real data in the form of a COPROD2 data set acquired in a flat earth environment. Using forward modeling, we have then demonstrated that the topography effect may become significant. A flat earth inversion of data generated from a homogeneous model including topography exhibits characteristic artifacts
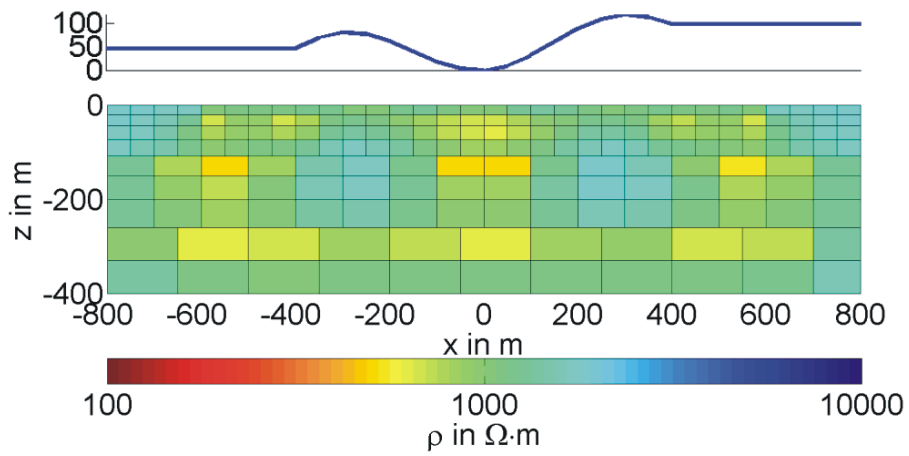
Figure 5: Flat earth inversion results of VLF-R data generated from a model including topography. For reasons of comparison, the original topography is plotted at the top.
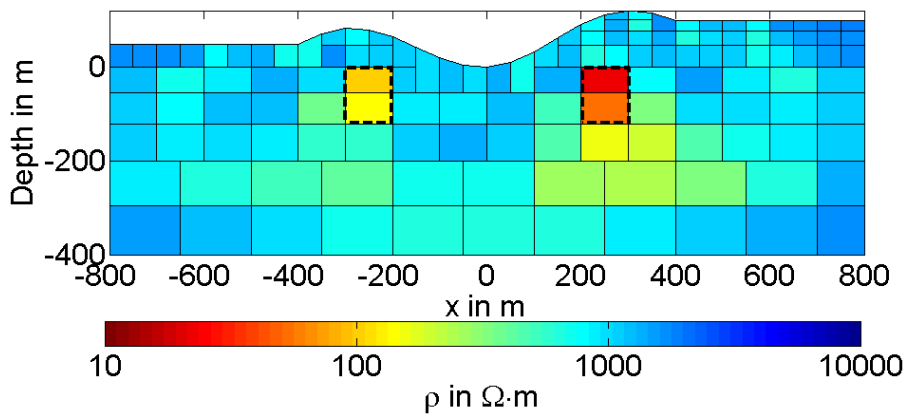

Figure 6: Inverted model obtained by inversion of VLF-R data using the rectangular/trapezoidal parameterization scheme.
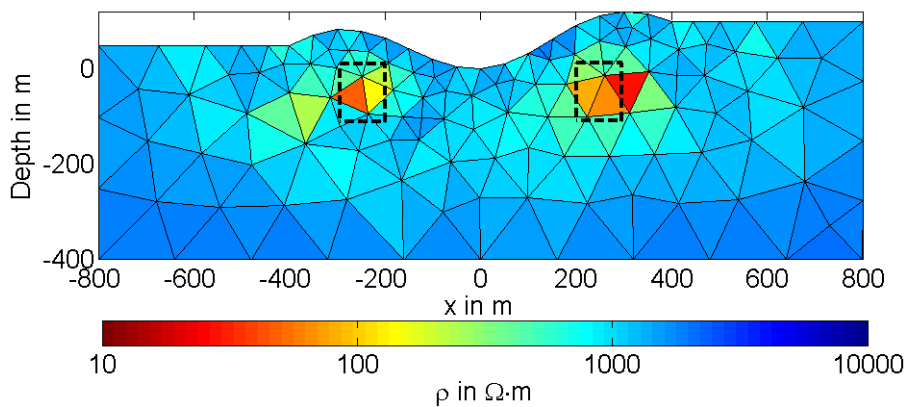

Figure 7: Inverted model obtained by inversion of VLF-R data using the unstructured parameterization scheme.

and, thus, corroborates the necessity to incorporate the topography into the inversion process.

After demonstrating the effect of topography, we have shown by inversion of VLF-R data that our code is able to resolve anomalous regions in the presence of topography. Two parameterization schemes are tested for models including topography. The best inversion results are obtaimed when the grid is adapted to the structures in the inverse model. Future inversion strategies will therefore incorporate adaptive parametrization schemes during the inversion process.

Concluding, the inversion of models including surface or subsurface topography, i.e., seabed topography, voids, mining galleries, tunnels, caves etc. opens up new ways for field surveys and specific applications and enhances the interpretation techniques available at present.

References

deGroot-Hedlin, C. and Constable, S. (1993). Occam's inversion and the North American Central Plains electrical anomaly. *J. Geom. Geoelec.*, *45*, 985-999.

Farquharson, C. and Oldenburg, D. (1996). Approximate sensitivities for the electromagnetic inverse problem. *Geophys. J. Int.*, *126*, 235-252.

Franke, A., Börner, R.-U. and Spitzer, K. (2004). 2D finite element modelling of plane-wave diffusive time-harmonic electromagnetic fields using adaptive unstructured grids. *Extended abstract, 17th Workshop on Electromagnetic Induction in the Earth, Hyderabad, India. www-document. http://www.emindia2004.org.*, *S.2-O.01*, 1-6.

Jones, A. (1993). The COPROD2 dataset: Tectonic setting, recorded MT data and comparison of models. *J. Geom. Geoelec.*, *45*, 933-955.

Rodi, W. L. (1976). A technique for improving the accuracy of finite element solutions for magnetotelluric data. *Geophys. J. R. Astr. Soc.*, *44*, 483-506.